RSC Advances

This article can be cited before page numbers have been issued, to do this please use: F. Zheng, S. Xu, Z. Yin, Y. Zhang and L. Lu, *RSC Adv.*, 2016, DOI: 10.1039/C6RA19334J.

View Article Online
DOI: 10.1039/C6RA19334J

Facile Synthesis of MOF-derived Mn_2O_3 Hollow Microspheres as Anode Materials for Lithium-ion Batteries

Fangcai Zheng,[a, b*] Shihao Xu,[a] Zhichen Yin[a], Yuanguang Zhang[a] and Lu Lu[**]

[a] Anhui Provincial Laboratory of Optoelectronic and Magnetism Functional Materials, School of Chemistry and Engineering, Anqing Normal University, Anqing 246011, PR China

[b] High Magnetic Field Laboratory, Hefei Institute of Physical Science, Chinese Academy of Science, Hefei 230031, PR China

ABSTRACT

In this article, we report a facile and scalable route for the fabrication of Mn_2O_3 hollow microspheres by direct pyrolysis of Mn-based metal-organic frameworks at 450 ^oC with a hating rate of 10 ^oC/min in air. The effect of the heating rate on the morphology of the final samples has been also investigated. When evaluated as an anode material for LIBs, these Mn_2O_3 microspheres exhibited a reversible and stable capacity of 582 mAh g^{-1} after 60 cycles at a current density of 100 mA g^{-1}. The improved capacity and excellent cycling stability of the as-prepared Mn_2O_3 microspheres could be attributed to the porously hollow structures, which can reduce diffusion length for lithium ions and electrons, and also can enhance structural integrity for buffering the volume expansion during the discharge/charge processes.

Key Words: MOFs; Mn_2O_3; Hollow structures; Lithium-ion batteries.

Introduction

Recently, manganese oxides (such as MnO, MnO_2, Mn_2O_3 and Mn_3O_4) are believed to be the most promising alternative anode materials for LIBs because of their earth-abundance, low cost, high specific theoretical capacity, and environmental benignity.[1-9] Furthermore, these Mn-based oxides exhibit higher output voltage and higher energy density due to their low operating voltages (1.3-1.5 V for lithium

* zfcai@mail.ustc.edu.cn **lulu19861117@126.com

View Article Online
DOI: 10.1039/C6RA19334J

extraction).[10] Among them, Mn_2O_3 has a high capacity of 1018 mAh g^{-1} and thus is considered to be potential anode materials for LIBs.[11] However, it has demonstrated that the Mn_2O_3 electrode exhibited poor cycling stability during the discharge/charge processes.[12] The Mn_2O_3 electrode easily suffers from the volume expansion, aggregation, and intrinsically low electrical conductivity during the discharge/charge processes, resulting in rapid capacity fading. As a consequence, several strategies have been used to solve the aforementioned problems for the Mn_2O_3 electrode. The mostly used one is to synthesize Mn_2O_3 with porous and hollow structures, in which vacant space provided by the structure can effectively accommodate the volume change and structural stain, shorten the diffusion path of lithium ions and electrons, and enlarge the contact area between the active materials and electrolyte during the discharge/charge processes.[13-16] However, the synthesis of Mn_2O_3 hollow structures usually involves tedious and complicated steps, expensive sacrificial templates, or time-consuming solvothermal reactions in autoclaves.[12] Thus, it is desirable to develop simple, scalable and economic approaches to synthesize Mn_2O_3 with hollow structures as anode materials for high-performance LIBs.

Metal-organic frameworks (MOFs) have attracted extensive research interest because of their diverse architectures and high surface area.[17-19] It has been demonstrated that MOFs can be used as promising templates or precursors to fabricate porous nanostructured materials *via* thermolysis.[21-24] For example Lou *et al.* has obtained Fe_2O_3 microboxes through direct calcination of prussian blue $Fe_4[Fe(CN)_6]_3$ in air.[25] Additionally, MOFs containing organic linkers can be also used as templates or precursors to develop a new class of porous functional materials.[26] For example, Cho *et al.* has used MOFs as a sacrificial template to fabricate several hollow and multi-ball-in-ball hybrid metal oxides by taking advantage of their unique reactivity and thermal behavior.[27] Yan and co-workers synthesized hollow silica nanocages using nanoscale MOFs as a template.[28] It was reported that the polyhedron-like and nanobar-like Mn_2O_3 have been fabricated with using MOFs as a template.[29, 30] Despite the progress achieved to date, research on the facile and scalable synthesis of hollow inorganic functional materials from MOFs is still in its very early stage.[31, 32] Moreover,

View Article Online
DOI: 10.1039/C6RA19334J

there has been rare success in fabricating Mn_2O_3 hollow microspheres with hierarchical structures due to additional difficulties from the lack of a proper MOF precursor. It is hence highly desirable to develop novel synthesis protocols and concepts to prepare Mn_2O_3 hollow microspheres with hierarchical structures through direct decomposition of rationally designed MOFs precursors.

In this article, we report a facile and scalable route for the fabrication of Mn_2O_3 hollow microspheres by direct pyrolysis of Mn-based metal-organic frameworks (denoted as Mn-BTC) at 450 ^{o}C with a hating rate of 10 ^{o}C/min in air. Moreover, a large number of O and C atoms uniformly dispersed in the Mn-BTC crystal structure can be also oxidized into gaseous molecules and escaped from the structure during the annealing process, which finally leads to porous structure. Furthermore, the effect of the heating rate on the morphology of the final samples has been also investigated. Combining the advantage of hollow hierarchical structures and nanopores within their structures, the as-prepared Mn_2O_3 hollow microspheres exhibited improved lithium-storage performance.

Experimental Section

Material preparation

All chemicals are of analytical grade, and were used without any further purification. Firstly, $Mn(CH_3COO)\cdot 4H_2O$ (49 mg) and PVP (K-30, 0.3 g) were dissolved in the mixed solution of C_2H_5OH and H_2O (5/5 ml) system under agitated stirring to give a transparent solution. Secondly, the mixed solution of C_2H_5OH/H_2O (5/5 ml) containing trimesic acid (90 mg) was added to the above solution slowly and regularly with a syringe (10 ml). After 10 min, the resulting solution was incubated at room temperature without any interruption for 24 h. The resulting white precipitates were collected by centrifugation, washed with ethanol threel times, and finally dried in an oven at 60 ^{o}C. The resulted samples with different morphologies were successfully obtained by thermal decomposition of Mn-BTC precursors at 450 ^{o}C for 2 h with different heating rates in air.

Material characterization

The powder X-ray diffraction (XRD) patterns of all samples were recorded with

View Article Online
DOI: 10.1039/C6RA19334J

a X-ray diffractometer (Japan Rigaku D/MAX-γA) equipped with Cu-Kα radiation (λ = 1.54178 Å). Field emission scanning electron microscopy (FE-SEM) images were collected on a JEOL JSM-6700 M scanning electron microscope. Transmission electron microscopy (TEM) images were taken on Hitachi H-800 transmission electron microscope using an accelerating voltage of 200 kV, and high-resolution transmission electron microscope (HRTEM) (JEOL-2011) was operated at an acceleration voltage of 200 kV. The specific surface area was evaluated at 77 K (Micromeritics ASAP 2020) using the Brunauer-Emmett-Teller (BET) method, while the pore volume and pore size were calculated according to the Barrett-Joyner-Halenda (BJH) formula applied to the adsorption branch. XPS measurements were performed on a VGESCALAB MKII X-ray photoelectron spectrometer with an Mg_{Ka} excitation source (1253.6 eV). Thermogravimetric analysis (TGA) was carried out using a Shimadzu-50 thermoanalyser under air flow.

Electrochemical measurements

The electrochemical performance of the Mn_2O_3 hollow microspheres was examined by using CR 2032 coin-type cells *versus* Li with 1 M $LiPF_6$ in the ethylene carbonate and diethyl carbonate (EC/DEC = 1:1, v/v) as the electrolyte. To prepare a working electrode, the as-prepared samples (80 wt%), conductive material (acetylene black, 10 wt%), and binder (polyvinylidene fluoride (PVDF), 10 wt%) were mixed in NMP, and the slurry was then pasted onto the surface of a copper foil current collector. The loading mass of an electrode is approximately 1 mg (1 mg/cm^2). The cells were assembled in an argon-filled glove box with both the moisture and the oxygen content bellow 1 ppm (Mikrouna, Super (1220/750/900)). The Li-storage performance was measured by a galvanostatic discharge-charge method in the voltage range between 0.01 and 3.0 V on a battery test system (Neware CT-3008W).

Results and discussion

View Article Online
DOI: 10.1039/C6RA19334J

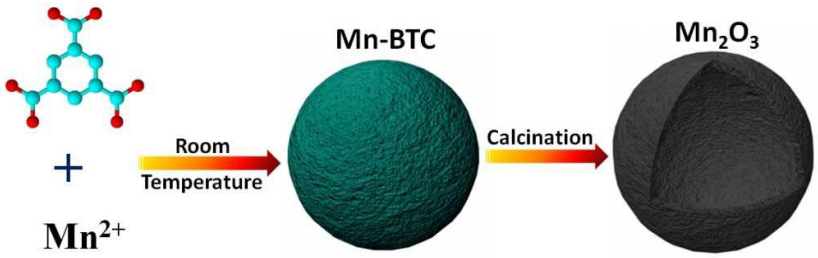

Figure 1. Schematic illustration for the formation of Mn_2O_3 hollow microspheres.

The strategy for the synthesis of Mn_2O_3 hollow microspheres with hierarchical structures is schematically depicted in Figure 1. First, an improved method was explored for synthesizing highly uniform Mn-BTC microspheres at room temperature. A subsequent thermal annealing process was then used to transform of the Mn-BTC precursor into Mn_2O_3 hollow microspheres. Compared with the wildly used solution- or template-based methods for creating hollow structures, the present solid-state approach provides a more facile route for the large-scale synthesis of hierarchically hollow microspheres.

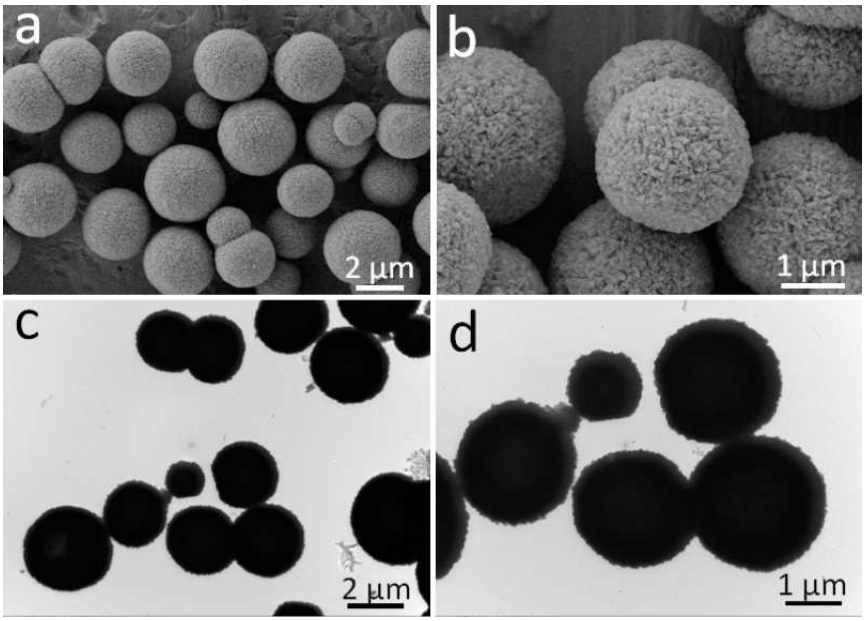

Figure 2. (a, b) FESEM and (c, d) TEM images of Mn-BTC precursors prepared at room temperature.

As shown in Figure 2a, it can be clearly observed that the precursor is composed of a great deal of microspheres with an average size of approximately 2 μm and exhibits rough surface. A close inspection (as shown in Figure 1b) reveals that the

View Article Online
DOI: 10.1039/C6RA19334J

microspheres are in fact assembled by small-size polyhedrons without serious aggregation. As shown in Figure 3, X-ray power diffraction (XRD) was also used to characterize the structure of the precursor, and the results confirmed the successful synthesis of the targeted Mn-BTC, according to the results reported by Lin's group.[33] In addition, the precursor was further characterized by thermogravimetric analysis (TG) in air. As shown in Figure 3b, the first step of weight loss started from room temperature to 200 ^{o}C, which can be attributed to the removal of physisorbed moisture or solvent molecules. A steep weight loss at 420 ^{o}C corresponds to the decomposition of the host frameworks (Mn-BTC). In order to ensure calcination of the Mn-BTC precursor completely, a temperature of 450 ^{o}C is chosen as the calcination temperature for the complete conversion of the Mn-BTC precursor to Mn_2O_3. Additionally, various heating rates was also applied to obtain the final samples with different morphologies and structures, hereinafter designated as Mn_2O_3-2R, Mn_2O_3-5R, and Mn_2O_3-10R, respectively(*e.g.,* "Mn_2O_3-2R" denotes a sample heated at 450 ^{o}C in air with a heating rate of 2 ^{o}C/min).

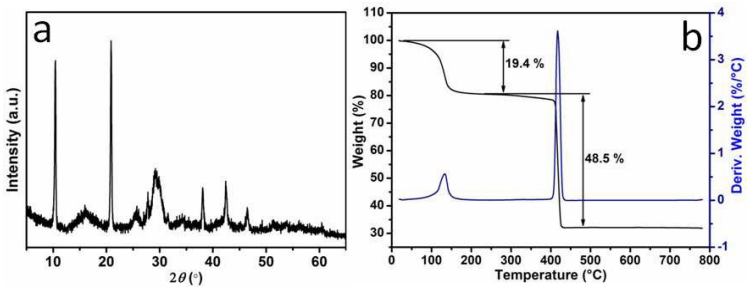

Figure 3. (a) XRD pattern and (b) thermogravimetric analysis (TGA) curves of Mn-BTC precursors.

The structure of the calcinated samples was further analyzed by XRD, and the results are shown in Figure 4. All of the peaks of the three samples can be indexed as the cubic Mn_2O_3 (JCPDS card no. 41-1442, lattice constant α = 9.409 Å). Therefore, it can be concluded that the Mn-BTC precursor was completely transformed into Mn_2O_3. However, the crystallinity of the as-prepared samples was improved with decreasing the heating rate. In order to get more information about the purity and chemical composition, the Mn_2O_3-10R was X-ray photoelectron spectroscopy (XPS). The

View Article Online
DOI: 10.1039/C6RA19334J

results confirm the co-existence of Mn and O in the structure, indicating high purity of the as-prepared sample. Figure 5 exhibits high-resolution XPS spectrum of Mn 2p. The Mn 2p orbital region exhibits the binding energies of Mn $2p_{1/2}$ and Mn $2p_{3/2}$ peaks at 653.1 and 641.2 eV, respectively.[34] The splitting energy of 1.9 eV between Mn $2p_{1/2}$ and Mn $2p_{3/2}$ is consistent with that of Mn_2O_3.[35] As shown in Figure S2b, the O 1s peaks at 529.6 and 531.0 eV can be attributed to the crystal lattice oxygen ($O_{Mn\text{-}O\text{-}Mn}$) and surface hydroxyl groups ($O_{H\text{-}O}$) in the Mn_2O_3, respectively.[36]

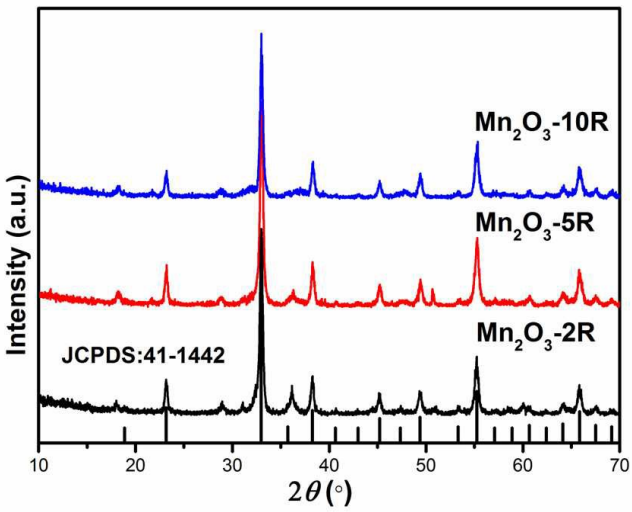

Figure 4. XRD patterns of as-prepared Mn_2O_3 samples obtained at different calcinated temperatures.

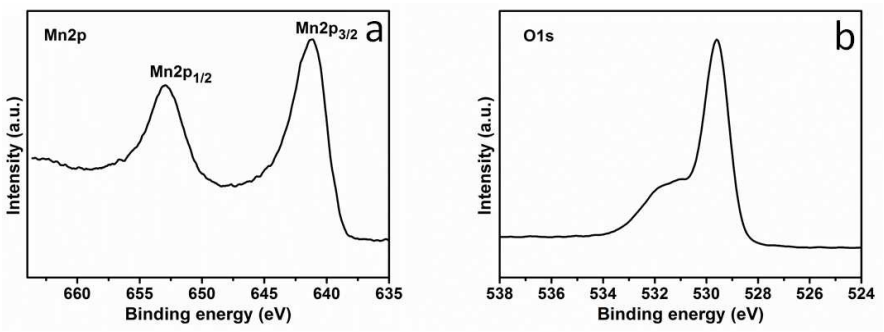

Figure 5. (a) Mn 2p and (b) O 1s XPS spectra of the as-prepared Mn_2O_3-10R.

The conversion of the Mn-BTC precursor to Mn_2O_3 was further investigated by FESEM and TEM, respectively. Figure 6a,b exhibit FESEM images at different magnifications of Mn_2O_3-10R. It can be clearly observed that Mn_2O_3-10R exhibits the pristine spherical shape with a porously hollow structure, and the surface of

View Article Online
DOI: 10.1039/C6RA19334J

Mn_2O_3-10R becomes rough, which can be attributed to the release of gaseous molecules (*e.g.* CO_2, H_2O) from the decomposition of Mn-BTC during the calcination process. Figure 4c shows a typical TEM image of Mn_2O_3-10R, and the sharp contrast between the centers and edges of spherical particles demonstrates a hollow structure for Mn_2O_3-10R. The hollow structure is mainly generated by heterogeneous contraction because of non-equilibrium heat treatment. The Mn-BTC precursor is not homogeneously heated during the heating process. Therefore, it exits a temperature gradient (ΔT) along the radial direction, resulting in the formation of a shell at the surface of the as-prepared precursor.[37] This shell is relatively rigid and can prevent the further contraction of the microspheres. At the same time, two forces of opposite directions exert at the interface of Mn-BTC core and Mn_2O_3 shell. The contraction force (F_c) facilitates the inward shrinkage of the core, while the adhesion force (F_a) induces the outward contraction. Moreover, a large amount of gaseous molecules (e. g. CO_2, H_2O) released from the decomposition of Mn-BTC core can also decrease F_c. Therefore, with a large ΔT and numerous gaseous molecules released, F_a would exceed F_c, resulting in hollow and porous structure of the as-prepared Mn_2O_3.[29, 34] The formation of Mn_2O_3 was investigated in detail by carrying out the decomposition of Mn_2O_3 under various heating rates. At a low heating rate of 5 and 2 $^oC\ min^{-1}$, the resulted sample show a broken hollow structure (SEM and TEM, Figure 7) with an improved crystallinity (XRD, Figure 4). In addition, a representative high-resolution TEM (HRTEM) image of Mn_2O_3-10R is shown in Figure 4d, the measured interplanar distance of a randomly selected single nanocrystal is 0.27 nm, which is in good agreement with the (222) plane of Mn_2O_3, thus confirming the XRD analysis.

View Article Online
DOI: 10.1039/C6RA19334J

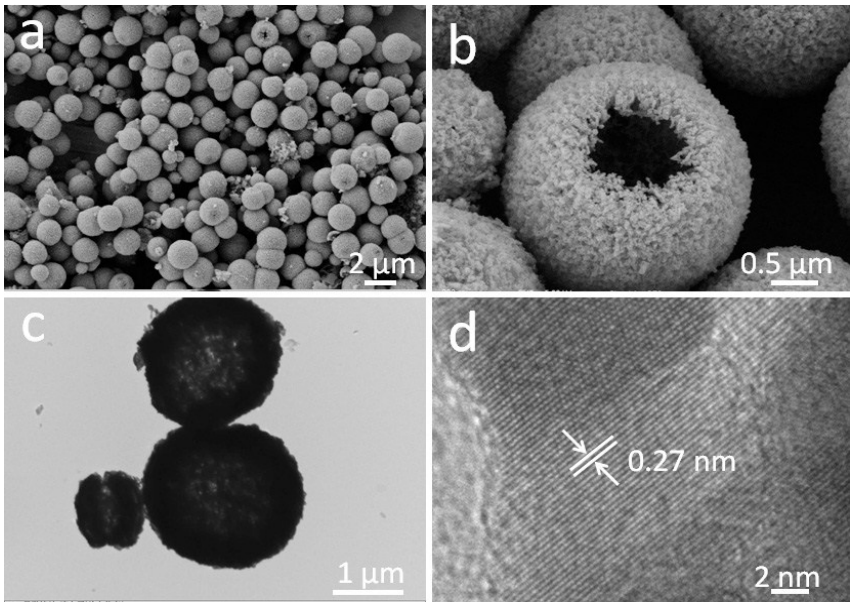

Figure 6. (a, b) FESEM images at different magnifications, (c) TEM image, and (d) HRTEM image of Mn_2O_3-10R.

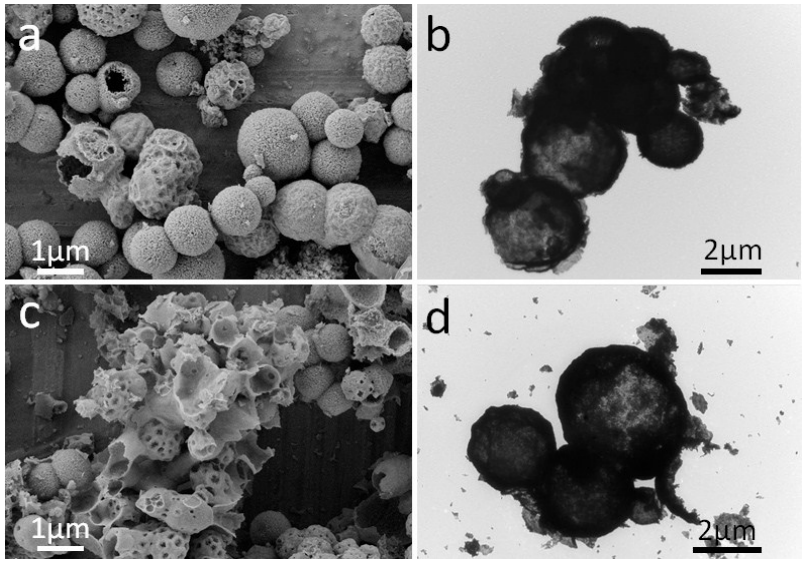

Figure 7. (a, b) SEM and TEM images of Mn_2O_3-5R and (c, d) SEM and TEM images of Mn_2O_3-2R.

To further investigate the specific surface area and the porous characteristic of the as-obtained samples, nitrogen adsorption-desorption isotherms were measured at 77K (Figure 8). The all isotherm profiles of the samples can be categorized as type Ⅱ curves with a H3 hysteresis loop at the relative pressure of 0.8-1.0, thus implying the existence of a large number of mesopores in the samples. Pore characteristics of

View Article Online
DOI: 10.1039/C6RA19334J

the as-obtained samples are shown in Table 1. It is noted that the special surface area of Mn_2O_3-10R (38.5 m^2 g^{-1}) is higher than other two samples (24.9 m^2 g^{-1} for Mn_2O_3-2R and 34.2 for Mn_2O_3-5R) obtained at relatively lower heating rates. In addition, the pore size distribution curve (the inset in Figure 8) obtained using Barrett-Joyner-Halenda (BJH) method reveals the pore size with a relatively wide distribution, which is consistent with the hollow structure observed by TEM. Based on previous reports, the porous structure might facilitate the fast transfer of lithium ions and electrons because the nanopores and interconnections provide a more favorable path for penetration and transportion of electrolytes.[38] Therefore, it is further suggested that the as-prepared Mn_2O_3-10R might be an excellent anode material for LIBs.

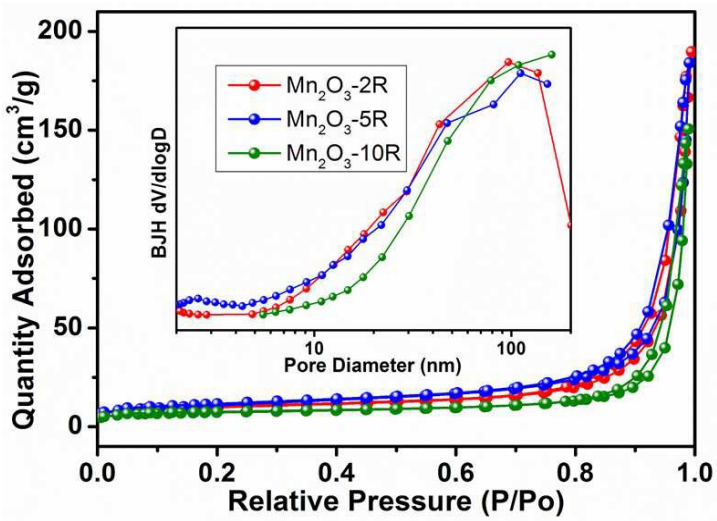

Figure 8. Nitrogen adsorption-desorption isotherms and the corresponding pore size distribution (inset) of the resulted samples.

Table 1. Summary of textural parameters obtained from nitrogen adsorption analysis.

Sample	S_{BET} (m^{-2} g^{-1})	Total pore volumes (cm^3 g^{-1})	Average pore size (nm)
Mn_2O_3-2R	24.9	0.1113	17.9
Mn_2O_3-5R	34.2	0.1689	19.8
Mn_2O_3-10R	38.5	0.1541	16.0

View Article Online
DOI: 10.1039/C6RA19334J

To study the performance and differentiation of the as-prepared Mn_2O_3 samples as anode materials of LIBs, the lithium-storage properties were investigated using the standard Mn_2O_3/Li half-battery configuration. Figure 9a shows representative cyclic voltammetry (CV) curves of the Mn_2O_3-10R electrode for the initial three cycles at a scan rate of 0.1 mV s^{-1} in the voltage range of 0.0-3.0 V *vs.* Li. In the first cycle, the two reduction peaks centered at approximately 1.2 and 0.9 V could be associated with the reduction of Mn^{3+} to Mn^{2+} and an irreversible reaction related to the lithium ion insertion of the conductive agent acetylene black, respectively.[7] Another main peak centered at approximately 0.2 V can be attributed to the further reduction of Mn^{2+} to Mn^0 along with the formation of Li_2O and the formation of a solid electrolyte interface (SEI) film.[39, 40] For the first anodic process, one broad peak locates at approximately 1.2 V, indicating the oxidation of Mn^0 to Mn^{2+}.[11] From the second cycle onwards, a shifting of the peak position is observed for the cathodic process, and the intensity of the peak drops significantly in the subsequent cycles relative to that in the first one, indicating the occurrence of some irreversible reactions with the decomposition of SEI film.[11, 39, 40] Based on above analysis and previous reports, the lithium storage mechanism of the Mn_2O_3 microspheres are believed to proceed as follows:[41, 42]

$$2\ Li^+ + 3\ Mn_2O_3 + 2\ e^- \rightarrow 2\ Mn_3O_4 + Li_2O \quad (1)$$

$$2\ Li^+ + Mn_3O_4 + 2\ e^- \rightarrow 3\ MnO + Li_2O \quad (2)$$

$$2\ Li^+ + MnO + 2\ e^- \rightarrow Mn + Li_2O \quad (3)$$

$$Mn + x\ Li_2O \leftrightarrow 2x\ Li^+ + MnO_x + 2x\ e^- \ (1.0 < x < 1.5) \quad (4)$$

Figure 9b shows the charge/discharge profiles of the Mn_2O_3-10R microspheres as anode materials for LIBs at a current density of 100 mA g^{-1} (0.08 mA cm^{-2}) in a potential window between 0.01 and 3.0 V. The general features of the charge/discharge profiles are consistent with other reported Mn_2O_3-based anodes that undergo redox reactions.[7, 42] In the first discharge profile, the voltage drops from 3.0 V to a voltage plateau at approximately 1.6 V, which can be attributed to the reduction of

View Article Online
DOI: 10.1039/C6RA19334J

Mn_2O_3 to Mn_3O_4 expressed by Equation (1). The voltage then further decreases to approximately 0.4 V with the formation of a new plateau. This can be associated to the reduction of Mn_3O_4 to MnO expressed by Equation (2). Lastly, the slow voltage drops to 0.01 V, expressed by Equation (3), indicating the complete reduction from Mn^{2+} to Mn^0. The initial discharge and charge capacities are found to be 3404 and 1559 mAh g^{-1}, respectively, leading to an initial coulombic efficiency of approximately 46 %. The relative low initial coulombic efficiency can be attributed to the formation of SEI film, the decomposition of electrolyte, and the reduction of adsorbed impurities on Mn_2O_3 surface.[43] This phenomenon also matches well with the CV results that the cathodic peaks are present in the first scan while absent afterward.

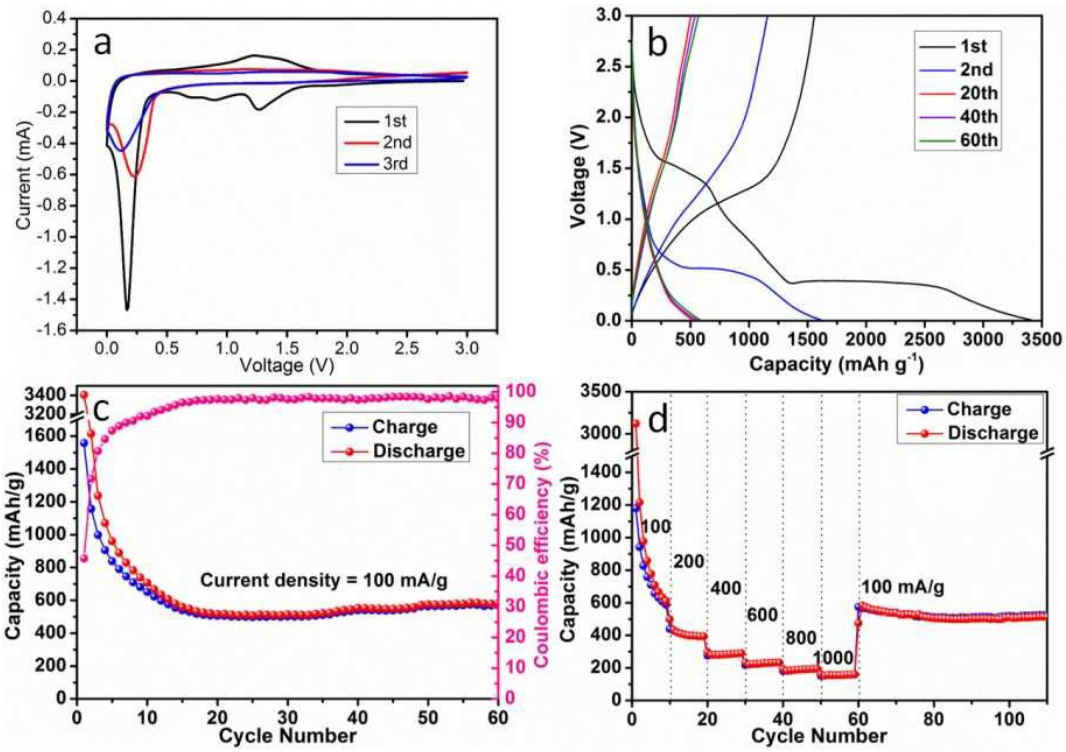

Figure 9. (a) Cyclic voltammetry measurements on Mn_2O_3-10R during the first three cycles. The voltage range was from 0.0 to 3.0 V at a scan rate of 0.1 mV s^{-1}. (b) Discharge-charge curves of Mn_2O_3-10R. The cell was test for 60 cycles between 0.1 mV and 3.0 V under a current density of 100 mA g^{-1} (0.08 mA cm^{-2}). (c) Cycle-life performance of Mn_2O_3-10R. (d) Rate capability test for the Mn_2O_3-10R at various current densities (100-1600 mA g^{-1}).

View Article Online
DOI: 10.1039/C6RA19334J

To evaluate the cycling stability, the Mn_2O_3-10R were charged and discharged at a current density of 100 mA g^{-1} over the voltage range of 0.01 - 3.0 V *vs* Li/Li^+, and the cycling performance is exhibited in Figure 9c. After 60 cycles, the discharge capacity is retained at 582 mAh g^{-1}. Moreover, from the 15th cycle onwards, the Mn_2O_3-10R sample shows the fascinating cycling stability with the coulombic efficiency over 97 %. Figure 9d exhibits the rate performance of the Mn_2O_3-10R sample by cycling the cell at various current densities. As the current density increased from 100 to 200, 400, 600, 800 and 1000 mA g^{-1}, the capacity decreased only from 611, 393, 290, 232, 195 to 160 mAh g^{-1}, respectively. When the current density was reduced from 1000 to 100 mA g^{-1}, a capacity of 513 mAh g^{-1} can be recovered, which has a trend to increase. Therefore, the as-prepared Mn_2O_3-10R sample exhibits an excellent electrochemical performance as an anode material for LIBs.

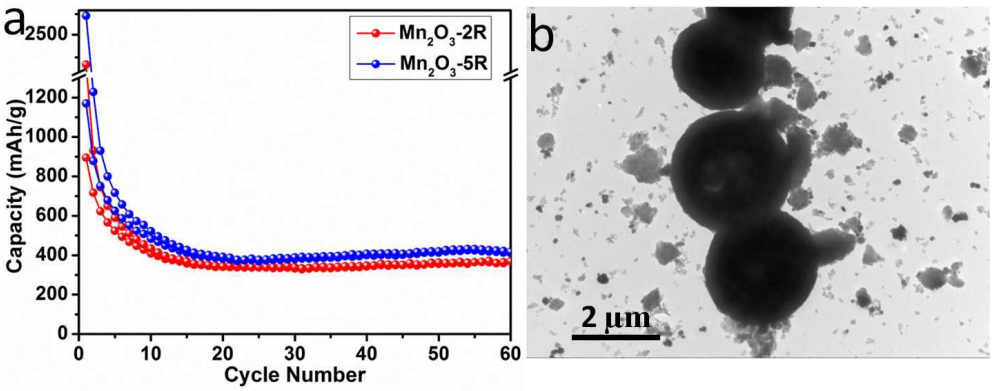

Figure 10. (a) Cycle-life performance of Mn_2O_3-5R and Mn_2O_3-2R at a current density of 100 mA g^{-1} (0.08 mA cm^{-2}), respectively. (b) The TEM image of Mn_2O_3-10R after charge/discharge processes.

In a control experiment, other two sample obtained at different conditions (Mn_2O_3-2R and Mn_2O_3-5R) were also investigated as anode materials for LIBs. As shown in figure 10a, both of them exhibit excellent cycling stability. However, compared with the capacity of the Mn_2O_3-10R, the lower capacities (369 mAh $g^{-1}$for Mn_2O_3-2R and 417 mAh g^{-1} for Mn_2O_3-5R) are retained at a current density of 100 mA g^{-1} after 60 cycles. Therefore, it is considered that the electrochemical

View Article Online
DOI: 10.1039/C6RA19334J

performance of Mn_2O_3-2R and Mn_2O_3-5R is not as good as that of Mn_2O_3-10R synthesized at 450 ^oC with a heating rate of 10 ^oC/min. In addition, as shown in figure 10b, the electrode materials (Mn_2O_3-5R) was investigated by TEM and the hollow microsphere structure can be well retained after charge/discharge processes. The excellent electrochemical performance of the Mn_2O_3-10R can be explained by its unique hollow structure with a variety features. Specifically, the void space within the hollow microsphere and the hierarchically porous shells provide abound channels and sites for efficient electrolyte penetration and enhance the contact area between the electrode and electrolyte. Meanwhile, such hierarchically hollow structures could also efficiently buffer the large volume changes induced by lithium insertion/extraction.

4. Conclusions

In summary, we have developed a facile and scalable strategy to synthesize Mn_2O_3 hollow microspheres with hierarchically porous shell structures, which contains the fabrication of Mn-BTC spherical template and subsequent one-step thermal annealing the template at moderate temperature in air. The effects of the heating rate on the morphology of the final samples have been also investigated and the resulted hollow microspheres may undergo a non-equilibrium inter-diffusion process. The resulted unique structure can facilitate the transport of lithium ions and electrons, and can also alleviate the volume changes during the discharge/charge processes, which ensure the improved electrochemical performance of the Mn_2O_3 electrode. When evaluated as anode materials for LIBs, the resulting Mn_2O_3 electrode exhibited a capacity of 582 mAh g^{-1} after 60 cycles at a current density of 100 mA g^{-1}. Furthermore, since MOFs can be synthesized with various compositions and morphologies, the MOFs-derived strategy can be extended to design and synthesis of other porously hollow metal oxides for applications in high-performance LIBs, supercapacitors, catalysts, and adsorbents in many scientific disciplines.

Acknowledgments

This work was supported by the National Natural Science Foundation (NSFC, 21601003, 21371009), Anhui Provincial Natural Foundation (No. 1608085QB34), the

View Article Online
DOI: 10.1039/C6RA19334J

Scientific Research Foundation of Anqing Normal University (044-150002021) and Natural Science Research Key Project of Anhui Provincial Department of Education (KJ2016A860).

References

(1) A. R. Armstrong, C. Lyness, P. M. Panchmatia, M. S. Islam and P. G. Bruce, *Nature Mater.,* 2011, **10**, 223-229.

(2) C. Z. Yuan, H. B. Wu, Y. Xie and X. W. Lou, *Angew. Chem. Int. Ed.,* 2014, **53**, 1488-1504.

(3) Y. Xia, Z. Xiao, X. Dou, H. Huang, X. H. Lu, R. J. Yan, Y. P. Gan, W. J. Zhu, J. P. Tu, W. K. Zhang and X. Y. Tao, *ACS Nano*, 2013, **7**, 7083-7092.

(4)Y. J. Zhang, Y. Yan, X. Y. Wang, G. Li, D. R. Deng, L. Jiang, C. Y. Shu and C. R. Wang, *Chem. Eur. J.*, 2014, **20**, 6126-6130.

(5) R. B. Wu, X. K. Qian, F. Yu, H. Liu, K. Zhou, J. Wei and Y. Z. Huang, *J. Mater. Chem. A,* 2013, **1**, 11126-11129.

(6) S. M. Guo, G. X. Lu, S. Qiu, J. R. Liu, X. Z. Wang, C. Z. He, H. G. Wei, X. R. Yan and Z. H. Guo, *Nano Energy,* 2014, **9**, 41-49.

(7) X. Zhang, Y. T. Qian, Y. C. Zhu and K. B. Tang, *Nanoscale*, 2014, **6**, 1725-1731.

(8) J. Zang, J. J. Chen, C. L. Zhang, H. Qian, M. S. Zheng and Q. F. Dong, *J. Mater. Chem. A,* 2014, **2**, 6343-6347.

(9) Y. N. Ko, S. B. Park, S. H. Choi and Y. C. Kang, *Sci. Rep.,* 2014, **4**, 5751.

(10) Y. M. Sun , X. L. Hu , W. Luo , F. F. Xia and Y. H. Huang , *Adv. Funct. Mater.,* 2013 , **23** , 2436-2444.

(11) S. Z. Huang, J. Jin, Y. Cai, Y. Li, Z. Deng, J. Y. Zeng, J. Liu, C. Wang, T. Hasan and B. L. Su, 2015, *Sci. Rep.,* 2014, **5**, 14686.

(12) G. R. Yang, W. Yan, J. N. Wang and H. H. Yang, *CrystEngComm,* 2014, **16**, 6907-6913.

(13) X. P. Shen, Z. Y. Ji, H. J. Miao, J. Yang and K. M. Chen, *J. Alloys Compd.,* 2011, **509**, 5672-5676.

(14) S. M. Oh, I. Y. Kim, S. J. Kim, W. Jung and S. J. Hwang, *Mater. Lett.,* 2013,

View Article Online
DOI: 10.1039/C6RA19334J

107 , 221-224.

(15) Y. C. Qiu, G. L. Xu, K. Y. Yan, H. Sun, J. W. Xiao, S. H. Yang, S. G. Sun, L. M. Jin and H. Deng, *J. Mater. Chem.,* 2011, **21**, 6346-6353.

(16) M. W. Xu, Y. B. Niu, S. J. Bao and C. M. Li, *J. Mater. Chem. A*, 2014, **2**, 3749-3755.

(17) A. Umemura, S. Diring, S. Furukawa, H. Uehara, T. Tsuruoka, S. Kitagawa, *J. Am. Chem. Soc.,* 2011, **133**, 15506-15513.

(18) J. K. H. Hui and M. J. MacLachlan, *Coord. Chem. Rev.,* 2010, **254**, 2363-2390.

(19) K. E. DeKrafft, C. Wang and W. B. Lin, *Adv. Mater.*, 2012, **24**, 2014-2018.

(20) S. J. Yang, S. Nam, T. Kim, J. H. Im, H. Jung, J. H. Kang, S. G. Wi, B. Park and C. R. Park, *J. Am. Chem. Soc.,* 2013, **135**, 7394-7397.

(21) R. B. Wu, X. K. Qian, X. H. Rui, H. Liu, B. L. Yadian, K. Zhou, J. Wei, Q. Y. Yan, X. Q. Feng, Y. Long, L. Y. Wang and Y. Z. Haung, *Small,* 2014, **10**, 1932-1938.

(22) F. C. Zheng, D. Q. Zhu, X. H. Shi and Q. W. Chen, *J. Mater. Chem. A,* 2014, **3**, 2815-2824.

(23) F. C. Zheng, G. L. Xia, Y. Yang and Q. W. Chen, *Nanoscale*, 2015, **7**, 9637-9645.

(24) F. C. Zheng, Y. Yang and Q. W. Chen, *Nat. Commun.,* 2014, **5**, 5261.

(25) S. Maiti, A. Pramanik and S. Mahanty, CrystEngComm, 2016, 18, 450-461.

(26) L. Zhang, H. B. Wu, S. Madhavi, H. H. Hng and X. W. Lou, *J. Am. Chem. Soc.,* 2012, **134**, 17388-17391.

(27) W. Cho, Y. H. Lee, H. J. Lee and M. Oh, *Adv. Mater.,* 2011, **23**, 1720-1723.

(28) N. Yan, F. Wang, H. Zhong, Y. Li, Y. Wang, L. Hu and Q. W. Chen, *Sci. Rep.,* 2013, **3**, 1568.

(29) K. Z. Cao, L. F. Jiao, H. Xu, H. Q. Liu, H. Y. Kang, Y. Zhao, Y. C. Liu, Y. J. Wang and H. T. Yuan, Adv. Sci., 2016, 3, 1500185.

(30) S. Maiti, A. Pramanik and S. Mahanty, CrystEngComm., 2016, 18, 450-461.

(31) F. C. Zheng, M. N. He, Y. Yang and Q. W. Chen, *Nanoscale,* 2015, **7**, 3410-3417.

(32) Y. L. Min, G. Q. He, Q. J. Xu and Y. C. Chen, J. Mater. Chem. A, 2014, 2, 2578-2584.

View Article Online
DOI: 10.1039/C6RA19334J

(33) K. M. L. Taylor, W. J. Rieterand and W. B. Lin, *J. Am. Chem. Soc*., 2008, **130**, 14358-14359.

(34) J. G. Kim, S. H. Lee, Y. Kim and W. B. Kim, *ACS Appl. Mater. Interfaces,* 2013, **5**, 11321–11328.

(35) G. Yang, Q. Zhang, W. Chang and W. Yan, *J. Alloys Compd.,* 2013, **580**, 29–36.

(36) G. R. Yang, W. Yan, J. N. Wang and H. H. Ynag, *CrystEngComm,* 2014, **16**, 6907-6913.

(37) S. M. Xu, C. M. Hessel, H. Ren, R. B. Yu, Q. Jin, M. Yang, H. J. Zhao and D. Wang, *Energy Environ. Sci.,* 2014, **7**, 632-637.

(38) L. Hu and Q. W. Chen, *Nanoscale,* 2014, **6**, 1236-1257.

(39) L. F. Xiao, Y.Y. Yang, J. Yin, Q. Li and L.Z. Zhang, *J. Power Sources,* 2009, **194**, 1089-1093.

(40)Y. Ren, A. R. Armsrong, F. Jiao and P. G. Bruce, *J. Am. Chem. Soc.,* 2010, **132** ,996-1004.

(41) B. C. Sekhar, G. Babu and N. Kalaiselvi, *RSC Adv.,* 2015, **5**, 4568-4577.

(42) L. Chang, L. Mai, X. Xu, Q. An, Y. Zhao, D. Wang and X. Feng, *RSC Adv.,* 2013, **3**, 1947–1952.

(43) X. F. Fang, X. Lu, X. W. Guo, Y. Mao, Y. S. Hu, J. Z. Wang, Z. X. Wang, F. Wu, H. K. Liu and L.Q. Chen, *Electrochem. Commun*., 2010, **12**, 1520-1523.